Meteoritics & Planetary Science 58, Nr 7, 1039–1055 (2023)
doi: 10.1111/maps.14026

Report

Micro-XCT chondrule classification for subsequent isotope analysis

Noah JÄGGI [1,2]*, Antoine S. G. ROTH[2], Miriam RÜFENACHT[2], Maria SCHÖNBÄCHLER [2], and André GALLI [1]

[1]Physikalisches Institut, University of Bern, Bern, Switzerland
[2]Institute für Geochemie und Petrologie, ETH Zürich, Zürich, Switzerland
*Correspondence
Noah Jäggi, Physikalisches Institut, University of Bern, Sidlerstrasse 5, CH-3012 Bern, Switzerland.
Email: noah.jaeggi@unibe.ch

(*Received 18 February 2022; revision accepted 20 May 2023*)

Abstract–Chondrules are microscopic, recrystallized melt droplets found in chondritic meteorites. High-resolution isotope analyses of minor elements require large enough element quantities which are obtained by dissolving entire chondrules. This work emphasizes the importance of X-ray computed tomography (XCT) to detect features that can significantly affect the bulk chondrule isotope composition. It thereby expands on other works by looking into chondrules from a wide range of chondrites including CR, CV, CB, CM, L, and EL samples before turning toward complex and time-consuming chemical processing. The features considered are metal and igneous rims, compound chondrules, matrix remnants, and metal contents. In addition to the identification of these features, computed tomography prevents the inclusion of non-chondrule samples (pure matrix or metal) as well as samples where two different chondrule fragments with potentially different isotope compositions are held together by matrix. Matrix surrounding chondrules is also easily detected and the affected chondrules can be omitted or reprocessed. The results strongly encourage to perform XCT before dissolution of chondrules for isotope analysis as a non-invasive method.

INTRODUCTION

Chondrules are the predominant component of most chondritic meteorites (Jones, 2012). They are crystallized melt droplets that formed in the protoplanetary disk by multiple, local heating events of precursor dusts or during impact events. They date back to the oldest solids—the calcium–aluminum-rich inclusions (CAIs)—which condensed out of the solar nebula 4.568 billion years ago (e.g., Bollard et al., 2017; Connelly et al., 2012; Desch et al., 2023; Piralla et al., 2023). Chondrules, CAIs, and other chondritic components including matrix and metal accreted into the chondrite parent bodies, which constitute leftover building blocks of planets. The characterizations of chondrites and their components provide powerful constraints on the earliest processes of planet formation in the protoplanetary disk (Connolly & Jones, 2016; van Kooten et al., 2021). However, often the material is rare and the carefully consideration of nondestructive methods is necessary. Moreover, it is paramount for the analysis of chondrules, that indeed only chondrule material is analyzed and this requires careful characterization of the material prior to further analyses. For example, a key feature is the bulk composition of chondrites. It represents the weighted average composition of their components. Each component may show distinct isotopic compositions depending on precursor materials and the conditions that prevailed at the time of formation. In the case of Ti isotopes, the isotopic compositions of single chondrules and their bulk host chondrites are strongly influenced by CAIs and amoeboid olivine aggregates (AOA), which display large excesses in ^{46}Ti and ^{50}Ti, inducing large variability within one chondrite (e.g., Allende, Gerber

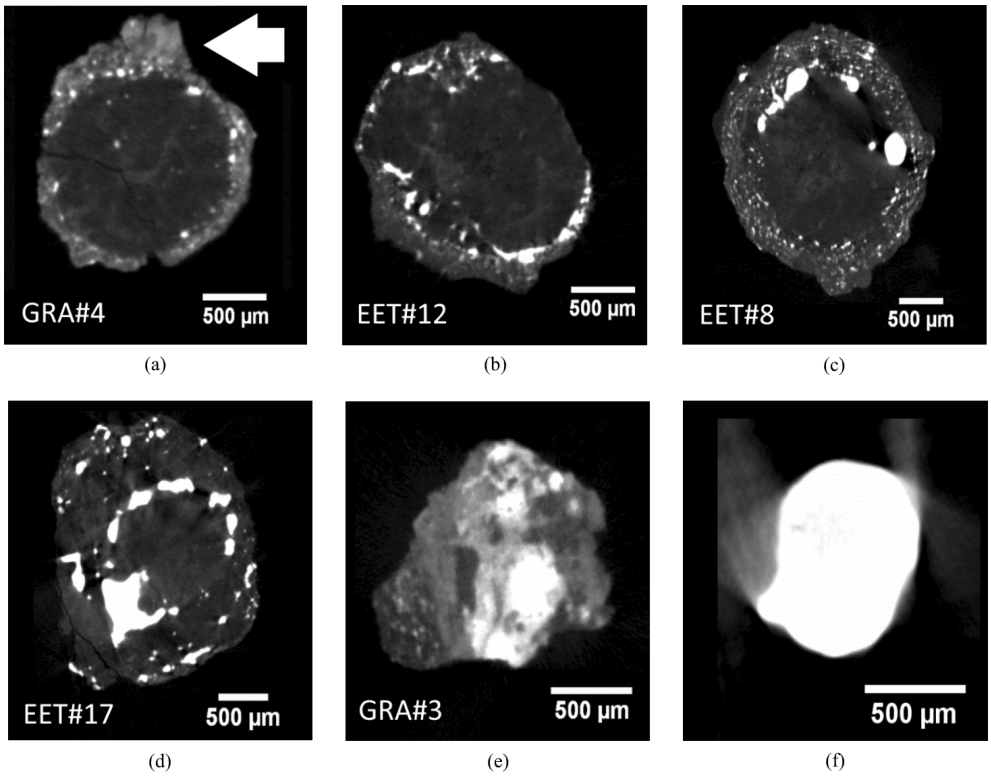

FIGURE 1. X-ray computed tomography images of chondrules expressing features including (a) matrix residue, (b) compound chondrule, (c) igneous rim, and (d) double (metal) rim or enveloping compound chondrule. Image (e) shows a sample made up of metal and matrix, whereas (f) shows metal. Both (e) and (f) were mistaken for a chondrule during sample selection. The highest attenuating features are shown as white (metal), and the lowest in black (air). Sample short forms correspond to chondrites extracted from EET 92048 and GRA 06100.33, respectively.

et al., 2017; Leya et al., 2009; Schneider et al., 2020; Trinquier et al., 2009; Williams et al., 2020). It is essential to distinguish between recycled CAI/AOA material that was incorporated into the chondrule (Marrocchi et al., 2018; Nagahara, 1981; Scott & Jones, 1990; Villeneuve et al., 2020) and the material that accidentally sticks to the surface of the chondrule.

Spatial resolution isotope analysis of major elements can reliably be performed in situ by secondary ion mass spectrometry (SIMS; Krot, 2019; Leshin et al., 1997, and references therein) or electron microprobe analysis (e.g., Ebel et al., 2008) using thick and thin sections. In contrast, large chondrule fragments, a whole chondrule or several chondrules pooled together (sample pooling) are dissolved in acids to obtain sufficient amounts of minor and trace elements (e.g., Ca, Ti, Cr, and Ni) for high-precision isotope analysis. The elements of interest are separated and concentrated using ion-exchange chromatography prior to isotope analysis using multicollector-inductively coupled plasma mass spectrometry (MC-ICPMS) or thermal ion mass spectrometry (TIMS; Schönbächler & Fehr, 2013). Several features in and around chondrules can have distinct isotope compositions compared to the initially formed chondrule. These features include (i) matrix (Gerber et al., 2017), (ii) compound chondrules (e.g., Arakawa & Nakamoto, 2016; Hubbard, 2015), (iii) coarse-grained igneous rims (e.g., Krot et al., 1995; van Kooten et al., 2021), and secondary metal rims (Jacquet et al., 2013). These are discussed in the following.

Matrix can remain attached to chondrules when chondrules are extracted from their host chondrite (Figure 1a, darker gray). Matrix and chondrules exhibit distinct chemical and isotopic characteristics as matrix is generally enriched in volatile elements compared to chondrules (e.g., Anders, 1964; Becker et al., 2015; Bland et al., 2005; Hezel, Bland, et al., 2018; Hezel, Harak, et al., 2018; Hezel, Wilden, et al., 2018; van Kooten et al., 2021; Zanda et al., 2012). For example, using the Ti isotope composition of a typical Allende matrix (1.91 ± 0.19 ε^{50}Ti; Gerber et al., 2017) and an Allende chondrule with a large ^{50}Ti excess (7.32 ± 0.03 ε^{50}Ti; Gerber et al., 2017). Mass balance calculations show that ε^{50}Ti of a contaminated chondrule sample composed of 2/3 chondrule and 1/3 matrix is about 25% lower than that of a non-contaminated chondrule sample.

Smaller matrix contamination is also critical to detect. One example provides nucleosynthetic variations in ε^{54}Cr. Here as little as 5 wt% Allende matrix (ε^{54}Cr = 1.06 ± 0.22, Schneider et al., 2020) shifts the lowest chondrule ε^{54}Cr data point of 0.09 reported in Schneider et al. (2020) to 0.14. Without systematic detection of matrix material, finding chondrule isotope compositions that greatly diverge from the expected mean is left to chance and the variability is underestimated. Other isotopes that are strongly affected by matrix are the He and Ne isotopes, relevant to cosmic ray exposure age dating. Both ^{3}He and ^{21}Ne are more abundant in the matrix compared to chondrules, affecting the isotopic ratios and lead to discordant exposure ages (Roth et al., 2016). Another application of matrix detection is the complementarity proposed for chondrules and matrix. It is suggested that both chondrules and matrix formed in the same reservoir (Hezel, Wilden, et al., 2018, and references therein), although this has been debated (e.g., Patzer et al., 2021; Zanda et al., 2018). To address this topic and detect, for example, chondrules that would not support the in situ formation of matrix, it is important to ascertain the absence of matrix during analysis that could falsify the result. For isotopes with narrow composition ranges, the contamination might seem less likely. However, unidentified cross-contamination will shift the measured data to the contamination values and limit the isotopic spread in the data. We conclude that detection of remnant matrix material on chondrules is important for representative bulk chondrule measurements, depending on the isotope system used.

Compound chondrules are aggregates of two or more chondrules that fused to form a single chondrule while remaining distinguishable (Figure 1b). To form a compound chondrule, chondrules either cooled down and solidified before fusing (Hubbard, 2015) or became supercooled melt droplets that crystallized upon collision (Arakawa & Nakamoto, 2016). In the special case, where compound chondrules exhibit interstitial matrix, the compound is thought to have formed on the chondrite parent body and not in space (i.e., Ebel & Rivers, 2007; Hezel et al., 2013). Moreover, a nested or enveloping chondrule (Wasson et al., 1995) shows a primary chondrule surrounded by a shell of a secondary chondrule (Rubin, 2010). Such enveloping shells might, however, be fine-grained igneous rims instead that are mistaken as compounds in XCT. The use of SEM X-ray maps of thick sections (e.g., Regnault et al., 2022) and chondrule fragments (Schneider et al., 2020; van Kooten et al., 2016) is a reliable tool for observing compounds that are observable in the chondrule midplane. However, we observed several compound chondrules which comprise of one large and several small chondrules, which are not detected in the chondrule midplane (see the Results section).

Jacquet (2021) suggested that the chondrules that build up the compound chondrules within the CO3 chondrites formed in the same gaseous medium. He based this conclusion on correlations between the volatile and moderately volatile element budgets of the single chondrules. In contrast, he observed distinct refractory element abundances between the chondrules, which he attributed to melting of independent nebular aggregates. Such distinct compositions are also expected for isotope composition and hence, bulk measurements of compound chondrules are unlikely to reflect the isotope signal of the single chondrule.

Chondrules of CV, CK, and CR chondrites often bear thick igneous rims formed from accreted dust generally exceeding 190 μm (Figure 1c; Abreu et al., 2020; Metzler et al., 1992; Rubin, 2010; Wasson & Rubin, 2010). Chondrules from ordinary chondrites (OC) and rumuruti chondrites (R, type 3) possess intermediate rim thicknesses with 150–160 μm and 120 μm, respectively, whereas CM, CO, EH, and EL chondrules only show thin rims of 30–60 μm. Several studies proposed that igneous rims are co-genetic with the chondrule and therefore should express a homogeneous isotopic composition (Friend et al., 2016; Libourel et al., 2006). van Kooten and Moynier (2019) showed that igneous rims of chondrules express δ^{66}Zn signals intermediate to the chondrule cores and chondrite matrix. More refractory elements such as the lithophile Ti are expected to remain immobile (Bauer et al., 2016) and thus should not equilibrate with surrounding matrix. The same way as with matrix of distinct isotopic composition, chondrules with thick igneous rims should be identified because they may not reflect the isotopic composition of the enclosed chondrule.

Double rim features are suggested to have either formed during an extended high-temperature event or by two subsequent heating and accretion events (Figure 1d; Jacquet et al., 2013; Schrader et al., 2008). A conflicting interpretation is that chondrules with two metal rims are instead enveloping compound chondrules, where a rigid chondrule was engulfed by a molten chondrule (Rubin, 2010; Wasson & Rubin, 2010; Wasson et al., 1995). The two chondrules thereby may or may not exhibit similar textures and compositions. The engulfing theory suggests the formation from two different melt batches and a potential homogenization of two isotope signals, which is not desired for single chondrule studies. Detection of multi-rim features is, however, the first step when striving to obtain isotopic data to support or reject the engulfing theory. High spatial resolution methods such as SIMS and/or microdrilling can be used to analyze the different layers of the chondrule

individually. For bulk analysis, double rim features should be avoided.

The final rim feature of relevance are the fine-grained dust rims, of unknown origins (both nebular and parent body processes are suggested, see Leitner et al., 2016, and references therein). They occur between the igneous chondrule rims and matrix. In XCT, the rims can be distinguished from matrix and chondrules, as previously shown (Hanna & Ketcham, 2018). We did not observe fine-grained rims around the chondrules analyzed in this work. This is likely due to the small differences in attenuation (Hanna & Ketcham, 2018), combined with the chondrule extraction process which generally does not preserve thick matrix envelopes. Fine-grained rims can possess a distinct isotope signal from the chondrule core (van Kooten et al., 2021). Mistaking a fine-grained rim for matrix or differentiating between them is not relevant for the purpose of this work, because both features are equally undesirable for isotope analysis.

A reliable way of classifying a chondrule is to analyze its features through one or several consecutive thick sections (i.e., Ebel et al., 2008). The classification scheme after Hewins (1997) considers (i) the FeO content of olivine (type I for Fa < 10, type II for Fa > 10), (ii) the modality of olivine and pyroxene (A for ol > 80%, AB for intermediate, and B for py > 80%), and (iii) the texture of the mineral grains (short forms: B = barred, R = radiating, P = porphyritic, MP = microporphyritic, G = granular). Thick sections offer a high reliability for the classification, however, the loss of material and potential contamination renders thick sections less desirable for subsequent bulk chondrule isotope analysis. Recent advances in microdrilling (e.g., van Kooten & Moynier, 2019; van Kooten et al., 2017) allow for direct powder extraction from thick sections previously characterized by SEM/EMP. Although showing a high potential, the microdrilling process often provides only small quantities of sample and can lead to measurements with low signal/noise ratios (e.g., van Kooten & Moynier, 2019). This is especially problematic for minor elements. Furthermore, the chemical separation procedure also requires optimization for small sample quantities to mitigate unwanted matrix and blank effects (Schönbächler & Fehr, 2013; van Kooten & Moynier, 2019). In summary, to mitigate these drawbacks, the capabilities and advantages of micro-X-ray computed tomography (XCT) as an analysis method without material loss prior to bulk dissolution are evaluated in this study.

A review on the method of micro-XCT and its application to planetary material is provided by Hanna and Ketcham (2017). The XCT method is fast, nondestructive, and boasts a high accessibility and ease of use. One batch of samples with 25 chondrules can be analyzed within a day, whereas the time needed to perform isotope analysis including time-consuming wet chemistry on the same batch may add up to several months. XCT is thus a potent and fast tool to identify chondrules without problematic features such as large matrix quantities or rims for further analysis. This way, the XCT data are valuable to support the interpretation of isotope data of the chondrules. Previous studies showed that spatial information such as the chondrule volume as well as the metal content can be obtained (Ebel et al., 2008; Hertz et al., 2003; Metzler, 2018; Metzler et al., 2019). Useful quantification and segmentation tools for metal and other opaques include PhaseQuant (Elangovan et al., 2012) and BLOB3D (Ketcham, 2005). A determination of the FeO content of olivine can be achieved with a monochromatic X-ray source (Gualda & Rivers, 2006; Uesugi et al., 2010, 2013). Nevertheless, the drawback of XCT is that it does not consistently allow to determine the petrological type of a chondrule (e.g., Uesugi et al., 2013). In contrast, the petrographic analysis (e.g., SEM) of a small section of a chondrule (e.g., Schneider et al., 2020) provides unambiguous results for classification; however, it cannot be used to fully assess the impact of potentially problematic features.

Unrelated to specific features, spherical samples extracted from chondrites are commonly identified as chondrules. Metal, matrix, and chondrule fragments bound by matrix can also occur in spherical shapes and can be mistaken as a chondrule (Figure 1e). The method of XCT has the power to identify such undesirable spherical objects. XCT has been used previously as a preliminary analysis tool prior to isotope analysis of, for example, chondrules from Murchison (CM2) (Hezel, Wilden, et al., 2018). This work now focuses on the systematic application of XCT to various carbonaceous and OC. It highlights the powerful information gained by XCT prior to dissolving the chondrule for isotope analysis which supports the processes of chondrule selection and isotope data interpretation.

METHODS

Samples

A total of 152 samples were extracted from Graves Nunataks (GRA 06100.33; CR2), Shişr 033 (CR), Elephant Moraine (EET 92048; CR2), Jbilet Winselwan (CM2), Allende (CV3), Gujba (CBa), Queen Alexandra Range (QUE 97008; L3.05), and Pecora Escarpment (PCA 91020; EL3) chondrites. They were separated from the meteorite using a hand drill with diamond heads and were hand-picked under an optical microscope. The sample holders for CT analyses are custom-made, hard plastic cylinders. They were rinsed with acetone and dried before adding fresh, ACS grade acetone (>99.9% purity,

ROMIL-SpS™) for about 10 min, followed by rinsing with Milli-Q water and drying. Transparent nail polish was used as an easily removable glue to stick the chondrules onto the sample holders. Chondrules were mounted onto each sample holder together with the pure reference minerals quartz and fluorite.

X-Ray Computed Tomography

Micro-XCT was performed using a Bruker Skyscan 1173, at the University of Lausanne, following the procedure and settings in Roth et al. (2016). The 70 keV polychromatic X-ray beam was pre-hardened using a 1.0 mm Al filter. No beam-hardening correction was applied. The low acceleration energy was chosen to maximize the sensitivity to variations on chemical composition to resolve chondrule textures with the caveat that opaques disproportionately attenuate the beam (e.g., Alles & Mudde, 2007; Zou et al., 2008). The calibration used pure, monocrystalline quartz, corundum, adularia, fluorite, and pyrite, to obtain an apparent effective energy (following Millner et al., 1978; Roth et al., 2016). The reference minerals on the holders served to convert gray scale to linear attenuation coefficients (LACs) at said effective energy of 20 keV. Note that the conversion from gray values to LACs is only qualitative with the goal to compare data from the different scanned holders. It fails in the presence of large opaque abundances (as discussed in Alles & Mudde, 2007; Zou et al., 2008). It is, however, useful for setting a uniform threshold in combination with the visual determination of chondrule types, as introduced below.

A voxel (3D equivalent of a pixel) with a side length of 5.3 μm was obtained by minimizing the sample to detector distance. The best compromise for time and quality yielded an exposure time of 700 ms, a step size of 0.23° with three averaged views per step. This resulted in a measuring time of about 55 min per sample holder. Larger exposure times and higher numbers of averaged views per step were tested, but did not notably increase the image quality to justify the significantly longer measuring times. Generally, 5–11 chondrules were measured with each sample holder which resulted in a large throughput of 25 chondrules per day on average.

For each stack, a full range reconstruction including all LACs in the chondrule and an export excluding metal LACs (white) was created. A smaller range thereby helps to preserve information as the LACs are binned into the 256 shades of gray of the 8-bit images. For the quality of XCT available, 8-bit images were sufficient to determine opaque contents and chondrule textures whilst keeping file sizes small. A full range reconstruction in 16 bit or 32 bit would avoid loss of information at the cost of size. Only the exports focusing on low LACs of silicates were used because they are required for chondrule classification. For the PCA 91020 chondrules, the full range reconstruction was used.

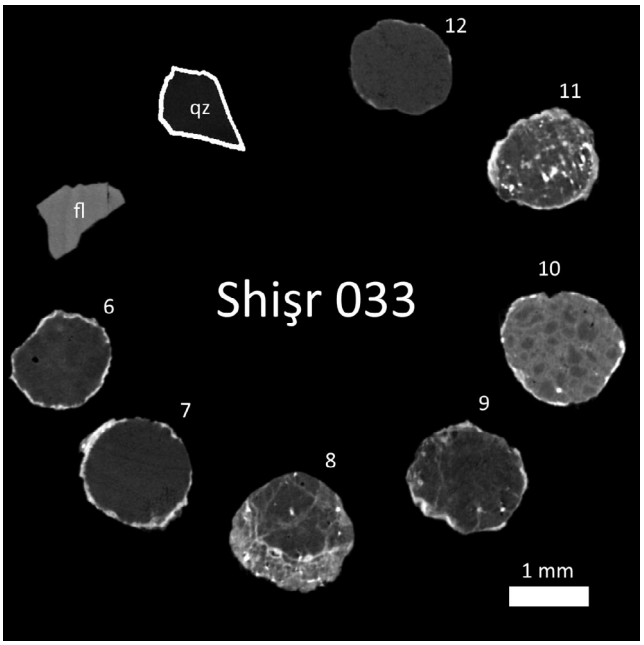

FIGURE 2. Shişr 033 chondrules #6–12 together with quartz (highlighted in white frame due to low attenuation) and fluorite used for calibration. Shişr #10, which appears brighter, is classified as a type II. A white rim was added to quartz (gz) for better visibility.

The general analysis procedure for metal content and chondrule volume follows Hertz et al. (2003), Ebel et al. (2008), and Elangovan et al. (2012). For chondrule-type determination, LAC histograms were employed as in Gualda and Rivers (2006) and Uesugi et al. (2010, 2013). Due to the attenuation sensitivity of the calibration, the LAC used to separate type I from type II chondrules exceeded the theoretical value calculated for Fa_{10} at the apparent effective energy of 20 keV (LAC $\simeq$ 13.5). A decrease of 2.5 keV in effective energy reduces the LAC of Fa_{10} to 20. We therefore determined type II chondrules visually by comparing them with other chondrules that had calibrated gray values. We also supported the detections using a threshold at a LAC of 20. The chondrules unambiguously determined as type II are much brighter compared with other chondrules on the same holder (Figure 2 and expressed LACs of $\geq$20.) The data analysis was performed in FIJI (**Fiji** **I**s **J**ust **I**mage**J**, Schindelin et al., 2012). The LACs of each XCT image stack were calibrated using the quartz and fluorite standards on the individual sample holders. Background (air), holder and glue LAC values were set to black by applying a threshold. One region of interest (ROI) was defined for each separate sample. The sample volume was

TABLE 1. Observed features in chondrule samples.

Chondrite		Chondrule											
			Type		Crystallinity					Rim		Other	
Type	Name	#	I	II	P	R	B	r.-less	?	Metal[a]	Ign.	Comp.[b]	Matrix
CR2	EET 92048	37	36	1 (3%)	15	0	0	3	19	20 (2)	7	7 (4)	7
CR2	GRA 06100.33	24	24	0	14	0	0	0	10	22 (1)	3	3 (3)	7
CR2	Shisr 033	21	18	3 (15%)	12	1	0	0	8	10 (1)	5	1 (1)	5
CV3	Allende	9	9	0	7	0	0	1	1	5	0	2 (0)	2
Cba	Gujba	9	9	0	0	0	0	0	9	0	0	0	1
CM2	Jbilet Winselwan	9	9	0	1	0	1	0	7	2	0	0	1
L3.05	QUE 97008	16	9	7 (43%)	3	3	1	0	9	4 (1)	2	0	4
EL3	PCA 91020	11	0	0	0	0	0	0	11	0	0	0	0
	Total	136										13 (8)	27

Note: Pure metal and pure matrix samples are excluded. Texture: P—porphyritic, R—radial, B—barred, ?—undefined. Features: rim-metal or igneous, comp.—compound chondrule; matrix—sample with matrix stuck to rim.
[a]The number of chondrules with a secondary metal rim is reported in the brackets.
[b]The number of compound chondrules separated by matrix is reported in the brackets.

obtained by counting the voxels inside a ROI. The equivalent radius was determined by assuming an ideal, spherical geometry.

The opaque contents were determined in *PhaseQuant* through clustering of gray values using the Kmeans procedure (Elangovan et al., 2012). To avoid a visual bias in thresholding, the MaxEntropy auto-threshold (Kapur et al., 1985) was applied to each ROI independently, resulting in a gray value between low attenuation silicates and high-attenuation opaques. In the case of particularly metal-poor chondrules, the auto-threshold setting was chosen based on a single image where the largest amount of metal was indicated. In addition, the auto-threshold method was not applied to the high-metal PCA 91020 chondrules due to the low silicate content resulting in a weak silicate peak. A value (17.2) close to the approximate LAC value separating type I from type II chondrules was chosen. The opaques troilite (FeS) and magnetite ($FeTiO_3$) have similar densities (Ebel & Rivers, 2007) and are not discriminable in our chondrule histograms, although their presence was detected as they attenuate more than silicates, but significantly less than metals. Metal was detected with a fairly high accuracy in chondrules with large metal nodules surrounded by "non-metal opaques" as shown in the ground truth measurement in Appendix A. For "rim-less" chondrules, where small opaque nodules are randomly distributed ("lithic fragment chondrules" in Hughes, 1978), the metal and non-metal opaque contents would bear large uncertainties. Therefore, only metal contents are reported except for chondrules labeled "rim-less," which is a small subgroup of all analyzed samples.

We found that the density of chondrules can be obtained from XCT data because LACs of reference chondrules (reference data not analyzed with XCT, Berlin, 2010) correlate with their respective bulk densities ρ (g cm^{-3}) with

$$\rho = \mathrm{LAC} \times 0.025 + 2.86. \quad (1)$$

The resulting densities reported in this work are expected to lie within 10% of their actual density. This accuracy was tested on 13 chondrules devoid of problematic features such as igneous rims by calculating the density from a measured mass and the respective XCT volume. For high-metal chondrules, the method is not applicable due to (a) neighboring effects, such as the partial volume effect, where information from a highly attenuating feature bleeds into adjoining voxels, increasing their apparent attenuation and (b) strong attenuation of X-rays by metal nodules causing starbursts—fan-like artifacts—and shadowing—due to extreme filtering of the beam (e.g., De Man et al., 1999; Hanna & Ketcham, 2017) increasing the mean LAC disproportionately and negatively affect the calibration process. The reported densities for chondrules without a very low or low metal content (<5 wt%) are thus likely erroneous.

RESULTS

The results from XCT, including chondrule types and textures, quantified properties as well as structural features are summarized in Tables 1 and 2. The extensive, chondrule-specific information is in Tables B1–B8 within the Appendix B. Out of the 152 scanned objects, 16 samples are not chondrules (i.e., Figure 1a–d) but either matrix (texture labeled as "matrix," Figure 1e) or pure metal nodules (texture reported as "metal," Figure 1f). The former also includes fragments of two or more

TABLE 2. Size (diameter) and metal content statistics of chondrule samples.

Chondrite		Chondrule							
		Size (mm)				Metal (vol%)			
Type	Name	Mean	Median	Min	Max	Mean	Median	Min	Max
CR2	EET 92048	1.27 (0.7)[a]	1.19	0.09	2.51 (2.9)[b]	4.8	2.8	0.0	27.9
CR2	GRA 06100.33	0.97 (0.7)[a]	0.84	0.50	1.85 (3.0)[b]	1.2	0.9	0.0	3.9
CR2	Shisr 033	1.68 (1.0)[c]	1.48	1.00	3.0	0.6	0.1	0.0	6.7
CV3	Allende	0.67 (0.9)[a]	0.56	0.48	1.12 (2.5)[d]	0.3	0.1	0.0	2.1
Cba	Gujba	11.4 (0.2)[a]	10.30	8.23	16.61 (15)[c]	1.0	0.1	0.0	4.0
CM2	Jbilet Winselwan	0.42 (0.3)[a]	0.40	0.27	0.60 (1.2)[c]	0.0	0.0	0.0	0.0
L3.05	QUE 97008	1.04 (0.6)[e]	1.02	0.59	1.48 (2.0)[b]	0.3	0.1	0.0	1.4
EL3	PCA 91020	0.74 (0.5)[a]	0.72	0.39	1.14 (1.8)[b]	71.5	71.1	61.6	82.1

Note: Pure metal and pure matrix samples are excluded.
[a]Reference data: Approximate mean size from sources found in Friedrich et al. (2015).
[b]Thin section analysis of chondrite (AMCD, 2022).
[c]Thin section analysis of chondrite (MBDB, 2022).
[d]Thick section analysis of chondrite. Largest chondrule size with a minimum of 80% circularity from Fisher (2014).
[e]XCT analysis of L chondrite Saratov from Metzler (2018).

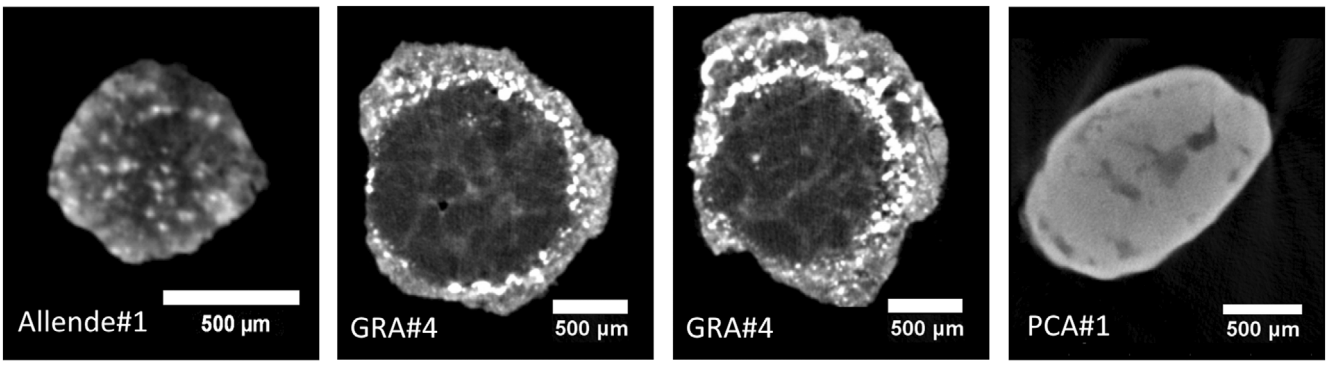

(a) (b) (c) (d)

FIGURE 3. (a) "Rim-less" chondrule; (b) metal and igneous rim; (c) slice of GRA#4 not situated at chondrule midplane which exposes multiple small adjoint chondrules; (d) typical metal-rich PCA 91020 chondrule.

chondrules connected by large amounts of matrix. Out of the 136 chondrules, the type of 118 could be determined (Table 1). The 11 chondrules from PCA 91020 could not be classified because of their high metal content and apart from metal surrounding mineral grains no further features are observable. Textures are predominantly porphyritic, but mostly not evident in XCT (labeled as tentative "†" or unknown "?").

The Jbilet Winselwan (CM2), Allende (CV3), and Gujba (CBa) chondrules yielded particularly low metal contents, whereas those of chondrules from the three CR chondrites and the L chondrite (QUE 97008) vary greatly (Table 2). A large variability of metal in chondrules from CR chondrites was previously reported by Ebel et al. (2008). Chondrules considered to be "lithic fragment chondrules" (Hughes, 1978) are labeled as "rim-less" (Figure 3a and Figure A1 in Appendix A). Their lack of rim features and a random distribution of small opaque nodules heavily implies that they did not experience metal migration and may have never been fully molten.

Chondrules with multiple metal rims are rare but occur in all three CR chondrites (EET 92048, GRA 06100.33, Shişr 033, Table 1, labeled as "m + m" in Appendix B, Figure 1d). Igneous rims were only detected for chondrules of the CR chondrites EET 92048, GRA 06100.33, Shişr 033, and the CM chondrite Jbilet Winselwan. Only three chondrules (from EET 92048 and GRA 06100.33) show a combination of metal and igneous rim (Figure 3b).

Compound chondrules (Figures 1b and 3c) are common in the CR chondrites EET 92048 (7/37 observations) and GRA 06100.33 (3/24) and were only

tentatively observed in the CV3 chondrite Allende (2/9) and Jbilet Winselwan (1/9) samples. No compound chondrules were found in QUE 97008 (0/18), PCA 91020 (0/11) and Gujba (0/9), and only one among the 21 analyzed Shişr 033 chondrules. Some compound chondrules with small chondrules attached to a larger chondrule could only be detected outside the chondrule midplane (compare Figure 3b to Figure 3c).

Apart from the three pure matrix samples, matrix remains on the rims of about 20% of all the chondrules after the initial mechanical separation from the chondrite (Figure 1a, Table 1). The 11 chondrules from PCA 91020 appear uniform and show large amounts of metal nodules within either a silicate metastasis or potentially porphyritic grains (Figure 3d). Their metal contents reach up to 82%.

DISCUSSION

Chondrule Metal Contents and Sizes

Metal contents were determined quantitatively, and reported for all chondrules except the rim-less samples (Appendix A). High (>20 vol%) metal contents reduce the expected mass of silicates and thus of lithophile elements such as Ti and Ni. Metal contents of PCA 91020 chondrules were very high and resulted in low Ti contents of the chondrules. Assuming ≤0.5 wt% Ti in the silicates (e.g., Williams et al., 2021), and a silicate density of 3.3 g cm^{-3} results in ≤0.15 μg Ti in the largest PCA#1 chondrule. This is not sufficient for high precision measurements, which generally require around 0.5 μg Ti (amount necessary depends on methodology and isotope). The knowledge on metal content is therefore essential for selecting chondrules for analysis and ensuring the required amounts of the desired isotopes.

The approximation of assuming a spherical chondrule when determining chondrule radii has proven accurate because it coincided well with measured radii as long as the sample was not fractured or angular. Our obtained radii should not be used for the determination of chondrule size distribution in the host chondrite. They were determined after mechanical chondrule extraction from the meteorite and therefore the data potentially have an intrinsic size bias dependent on chondrule friability (methodology of Metzler, 2018; Metzler et al., 2019). This is likely expressed in the smallest chondrules extracted from their parent chondrite either coinciding or exceeding the suggested mean sizes from literature data (Table 2). The exceptions are the chondrules extracted from Gujba, where our mean chondrule sizes greatly exceed the tabulated mean sizes, and those from Allende, with a mean slightly below the suggested 0.9 mm for CV chondrites.

Feature Detection

Our results demonstrate that matrix is easily detected using micro-XCT (Figure 1) and affects 20% of all extracted chondrules (Table 1). This information is relevant for future analysis to avoid such matrix contamination as outlined in the introduction. After identification, the matrix could possibly be mechanically removed and the chondrule re-scanned in XCT to verify clean removal (e.g., abrasion of extracted chondrules as performed by Roth et al., 2016).

Compound chondrules are reliably detected by XCT (Figure 1b). Small chondrules attached to a large chondrule (Figure 3b,c) are not evident when only analyzing the chondrule midplane using, for example, an SEM. This illustrates the value of XCT compared with more qualitative analysis methods such as thick sections or SEM petrographic analysis of a small fraction of a chondrule (e.g., Schneider et al., 2020). Excluding PCA 91020 chondrules, about 10% of all chondrules analyzed in this work are compound chondrules, a majority of which are separated by matrix (Table 1). A particularly large fraction (19%) of compound chondrules was found in Allende. This stands in stark contrast to the 1.75% identified by Hezel et al. (2013), where 400 chondrules were studied, or the 1.6% and 0.4% in the CV chondrites Allende and Axtell, respectively (Akaki & Nakamura, 2005) or the overall compound chondrule abundance in OC (L, L/LL, and LL) of 2.4% (Wasson et al., 1995). Our work was strongly biased toward large specimen for subsequent isotope analysis; therefore, the high abundance of compound chondrules likely reflects an artificial bias or sample heterogeneity. Evidently, compound chondrules are not desired for single chondrule isotope analysis and care must be taken to avoid them.

Metal and igneous rim features around chondrules are also reliably detected in XCT. We observed 5% and 10% double metal rim chondrules in our relatively small number of CR and OC chondrules, respectively (Table 1). For comparison, Rubin (2010) observed 1.4% and 0.2% of chondrules in CR and OC with inner and outer concentric metal rims. These, however, were considered to be "enveloping compound chondrules." Our results might again have an inherent sample bias due to extraction and selection. Following the motivation in the introduction, single and multi-rim features were omitted in the consecutive isotope analysis work.

The samples labeled "rim-less" with an absence of rim features and a random distribution of small metal nodules were only observed in three EET 92048 chondrules and tentatively in one Allende chondrule. It is likely that increasingly processed, spherical chondrules are more robust and thus more likely to be separated as a

chondrule for isotope analysis. This may lead to an over-representation in this work. The low degree of reprocessing (Varley et al., 2003; Zanda et al., 2002) renders "rim-less" chondrules a primary target for isotope analysis. The two caveats are that the metal contents and thus the desired element abundances (tied to silicates) are more difficult to predict for "rim-less" chondrules and that other potential contaminants such as relict grains (Jones, 2012; Russell et al., 2005) within "rim-less" chondrules are hard if not impossible to identify with our setup.

Classification

For classification purposes, chondrule textures could occasionally be determined (Table 1; Appendix B). Barren, porphyritic and radial textures were sometimes resolved (e.g., Figure 1a, Tables B5 and B8), whereas granular textures could be mistaken as porphyritic. The occurrence of nodules and mineral-crosscutting veins containing FeNi metal and Fe oxides caused artifacts (partial volume effect, starbursts and shadowing, e.g., De Man et al., 1999; Hanna & Ketcham, 2017) that complicated texture analysis in many cases. Furthermore, the artifacts can shift the LAC of the bulk chondrule histogram silicate peak to higher values, which increases the uncertainty on the chondrule-type classification. This was especially apparent in small, metal-rich "rim-less" chondrules (Figure 3a). The distribution of types is summarized in Table 1 and shows carbonaceous and enstatite chondrites with few to no type II chondrules with higher abundances in the OC QUE 97008, as expected (e.g., Rubin, 2010, and references therein).

Scanning the chondrules with a polychromatic beam at two distinctive effective energies potentially provides a higher probability of successfully differentiating between different phases and thus to observe the crystalline structure (e.g., Alves et al., 2014; Hanna & Ketcham, 2017; Van Geet et al., 2000). This was not applied in this study, because of time restraints. Moreover, success is not guaranteed, because insurmountable issues can occur from the polychromatic beam and beam hardening (e.g., Alves et al., 2014; Hanna & Ketcham, 2017; Van Geet et al., 2000). Obtaining high-quality data requires a monochromatic beam at a synchrotron facility (Tsuchiyama et al., 2013; Uesugi et al., 2013), which is not trivial and exceeds the scope of this and many other studies that require a quick sample characterization prior to isotope analysis. However, it would allow an unambiguous classification of the scanned chondrules, which then warrants the inclusion in larger data sets such as the *ChondriteDB* (Hezel, Harak, & Libourel, 2018).

CONCLUSIONS AND OUTLOOK

The power of XCT analyses is demonstrated by the number of chondrules affected by non-desirable features that were rejected from subsequent isotope analysis. Micro-XCT analyses detect metal rims, multi-rim features, and compound chondrules reliably, including matrix remnants from incomplete sample extraction. In numbers, 53 chondrules (35% of 152 extracted samples) showed one or more undesirable features, including 16 non-chondrule samples, 14 double rim chondrules, 11 chondrules with very high metal contents (PCA 91020), 13 compound chondrules, and 27 chondrules with matrix attached. It is noteworthy that most chondrules deemed not suitable for isotope analyses often exhibited a mixture of these features (e.g., GRA#4 with matrix and adjoined compound chondrules in Figures 1 and 3, respectively), potentially influencing the pristine chondrule isotope composition. The determination of chondrule type is generally possible visually, however, ambiguity exists for thresholding due to the attenuation of polychromatic X-rays working against calibration efforts (Alles & Mudde, 2007; Zou et al., 2008). Textures including barred, porphyritic, and radial can be resolved, whereas granular textures can be mistaken as porphyritic. Metal contents are easily obtained using CT, but they are often underestimated, in particular if metal is only present as small nodules and evenly distributed within the chondrule.

Polychromatic, single energy XCT does not allow for a clear chondrule classification but excels in feature recognition and adds constraints for interpretation of deviating isotope data. It also allows for a more informed selection of chondrules before sample dissolution and time consuming isotope analysis. The absence of any feature that could potentially interfere with the chondrule isotope compositions leads to better understood, robust data.

Acknowledgments—This work has been carried out within the framework of the National Centre of Competence in Research Planets supported by the Swiss National Science Foundation under grants 200021 L18277/1, 51NF40 182901, and 51NF40 205606. Special thanks to Romy D. Hanna from the Jackson School of Geosciences (Texas) for her repeated expert feedback, Benita Putlitz and Lukas Baumgartner from Geopolis Lausanne for their allocation of the XCT tomograph equipment and their support, Christian Liebske, Manuela Fehr (lab support), and Irene Ivanov (chondrule extraction) from ETH Zurich, Beda Hofmann, curator of the meteorite collection of the Natural History Museum of Bern for providing the Shişr 033 samples, and to the Antarctic Search for Meteorites (ANSMET) program,

for supplying the EET 92048, GRA 06100.33, QUE 97008, and PCA 91020 samples. US Antarctic meteorite samples are recovered by the Antarctic Search for Meteorites (ANSMET) program which has been funded by NSF and NASA, and characterized and curated by the Department of Mineral Sciences of the Smithsonian Institution and Astromaterials Curation Office at NASA Johnson Space Center. Open access funding provided by Eidgenossische Technische Hochschule Zurich.

Data Availability Statement—The data that support the findings of this study are openly available in Zenodo at http://doi.org/10.5281/zenodo.6109826.

Editorial Handling—Dr. Yves Marrocchi

REFERENCES

Abreu, N. M., Aponte, J. C., Cloutis, E. A., and Nguyen, A. N. 2020. The Renazzo-Like Carbonaceous Chondrites as Resources to Understand the Origin, Evolution, and Exploration of the Solar System. *Geochemistry* 80: 125631.

Akaki, T., and Nakamura, T. 2005. Formation Processes of Compound Chondrules in CV3 Carbonaceous Chondrites: Constraints from Oxygen Isotope Ratios and Major Element Concentrations. *Geochimica et Cosmochimica Acta* 69: 2907–29.

Alles, J., and Mudde, R. F. 2007. Beam Hardening: Analytical Considerations of the Effective Attenuation Coefficient of X-Ray Tomography. *Medical Physics* 34: 2882–9.

Alves, H., Lima, I., and Lopes, R. T. 2014. Methodology for Attainment of Density and Effective Atomic Number Through Dual Energy Technique Using Microtomographic Images. *Applied Radiation and Isotopes* 89: 6–12.

AMCD (2022). *Antarctic Meteorite Classification Database*. Antarctic Meteorites, Antarctic Meteorite Classification Database Website, NASA. https://curator.jsc.nasa.gov/antmet/classdb.cfm

Anders, E. 1964. Origin, Age, and Composition of Meteorites. *Space Science Reviews* 3: 583–714.

Arakawa, S., and Nakamoto, T. 2016. Compound Chondrule Formation Via Collision of Supercooled Droplets. *Icarus* 276: 102–6.

Bauer, K. K., Schönbächler, M., Fehr, M. A., Vennemann, T., Chaumard, N., Zanda, B., Bauer, K. K., et al. 2016. Titanium and Oxygen Isotope Compositions of Individual Chondrules from Ordinary Chondrites. 79th Annual Meeting of the Meteoritical Society, 7–12 August, Berlin, Germany. LPI Contribution No. 1921.

Becker, M., Hezel, D. C., Schulz, T., Elfers, B. M., and Münker, C. 2015. Formation Timescales of CV Chondrites from Component Specific Hf–W Systematics. *Earth and Planetary Science Letters* 432: 472–82.

Beitz, E., Blum, J., Mathieu, R., Pack, A., and Hezel, D. C. 2013. Experimental Investigation of the Nebular Formation of Chondrule Rims and the Formation of Chondrite Parent Bodies. *Geochimica et Cosmochimica Acta* 116: 41–51.

Berlin, J. 2010. Mineralogy and Bulk Chemistry of Chondrules and Matrix in Petrologic Type 3 Chondrites: Implications for Early Solar System Processes. In *Earth and Planetary Sciences ETDs*. Dissertation, University of New Mexico, Albuquerque. p. 234.

Bland, P. A., Alard, O., Benedix, G. K., Kearsley, A. T., Menzies, O. N., Watt, L. E., and Rogers, N. W. 2005. Volatile Fractionation in the Early Solar System and Chondrule/Matrix Complementarity. *Proceedings of the National Academy of Sciences of the United States of America* 102: 13755–60.

Bollard, J., Connelly, J. N., Whitehouse, M. J., Pringle, E. A., Bonal, L., Jørgensen, J. K., Nordlund, A., Moynier, F., and Bizzarro, M. 2017. Early Formation of Planetary Building Blocks Inferred from Pb Isotopic Ages of Chondrules. *Science Advances* 3, 1–9.

Connelly, J. N., Bizzarro, M., Krot, A. N., Nordlund, A., Wielandt, D., and Ivanova, M. A. 2012. The Absolute Chronology and Thermal Processing of Solids in the Solar Protoplanetary Disk. *Science* 338: 651–5.

Connolly, H. C., and Jones, R. H. 2016. Chondrules: The Canonical and Noncanonical Views. *Journal of Geophysical Research: Planets* 121: 1885–99.

De Man, B., Nuyts, J., Dupont, P., Marchal, G., and Suetens, P. 1999. Metal Streak Artifacts in X-Ray Computed Tomography: A Simulation Study. *IEEE Nuclear Science Symposium and Medical Imaging Conference* 3: 1860–5.

Desch, S. J., Dunlap, D. R., Dunham, E. T., Williams, C. D., and Mane, P. 2023. Statistical Chronometry of Meteorites. I. A Test of ^{26}Al Homogeneity and the Pb-Pb Age of the Solar System's t=0. *Icarus* 402: 115607.

Ebel, D. S., and Rivers, M. L. 2007. Meteorite 3-D Synchrotron Microtomography: Methods and Applications. *Meteoritics & Planetary Science* 42: 1627–46.

Ebel, D. S., Weisberg, M. K., Hertz, J., and Campbell, A. J. 2008. Shape, Metal Abundance, Chemistry, and Origin of Chondrules in the Renazzo (CR) Chondrite. *Meteoritics & Planetary Science* 43: 1725–40.

Elangovan, P., Hezel, D. C., Howard, L., Armstrong, R., and Abel, R. L. 2012. PhaseQuant: A Tool for Quantifying Tomographic Data Sets of Geological Specimens. *Computers & Geosciences* 48: 323–9.

Fisher, K. R. 2014. Contrasting Size Distributions of Chondrules and Inclusions in Allende CV3 Lunar and Planetary Science Conference, 2, The Woodlands, TX.

Friedrich, J. M., Weisberg, M. K., Ebel, D. S., Biltz, A. E., Corbett, B. M., Iotzov, I. V., Khan, W. S., and Wolman, M. D. 2015. Chondrule Size and Related Physical Properties: A Compilation and Evaluation of Current Data Across all Meteorite Groups. *Geochemistry* 75: 419–43.

Friend, P., Hezel, D. C., and Mucerschi, D. 2016. The Conditions of Chondrule Formation, Part II: Open System. *Geochimica et Cosmochimica Acta* 173: 198–209.

Gerber, S., Burkhardt, C., Budde, G., Metzler, K., and Kleine, T. 2017. Mixing and Transport of Dust in the Early Solar Nebula as Inferred from Titanium Isotope Variations among Chondrules. *The Astrophysical Journal Letters* 841: L17.

Gualda, G. A., and Rivers, M. 2006. Quantitative 3D Petrography Using X-Ray Tomography: Application to Bishop Tuff Pumice Clasts. *Journal of Volcanology and Geothermal Research* 154: 48–62.

Hanna, R. D., and Ketcham, R. A. 2017. X-Ray Computed Tomography of Planetary Materials: A Primer and Review of Recent Studies. *Geochemistry* 77: 547–72.

Hanna, R. D., and Ketcham, R. A. 2018. Evidence for Accretion of Fine-Grained Rims in a Turbulent Nebula for CM Murchison. *Earth and Planetary Science Letters* 481: 201–11.

Hertz, J., Ebel, D. S., and Weisberg, M. K. 2003. Tomographic Study of Shapes and Metal Abundances of Renazzo Chondrules Lunar and Planetary Science Conference, p. 1959.

Hewins, R. H. 1997. Chondrules. *Annual Review of Earth and Planetary Sciences* 25: 61–83.

Hezel, D. C., Bland, P. A., Palme, H., Jacquet, E., and Bigolski, J. 2018. Composition of Chondrules and Matrix and their Complementary Relationship in Chondrites. In *Chondrules: Records of Protoplanetary Disk Processes*, chapter 4, edited by S. Russell, Jr., H. C. Connolly, and A. Krot, 91–121. Cambridge, UK: Cambridge University Press.

Hezel, D. C., Elangovan, P., Viehmann, S., Howard, L., Abel, R. L., and Armstrong, R. 2013. Visualisation and Quantification of CV Chondrite Petrography Using Micro-Tomography. *Geochimica et Cosmochimica Acta* 116: 33–40.

Hezel, D. C., Harak, M., and Libourel, G. 2018. What We Know about Elemental Bulk Chondrule and Matrix Compositions: Presenting the Chondrite DB Database.

Hezel, D. C., Wilden, J. S., Becker, D., Steinbach, S., Wombacher, F., and Harak, M. 2018. Fe Isotope Composition of Bulk Chondrules from Murchison (CM2): Constraints for Parent Body Alteration, Nebula Processes and Chondrule-Matrix Complementarity. *Earth and Planetary Science Letters* 490: 31–9.

Hubbard, A. 2015. Compound Chondrules Fused Cold. *Icarus* 254: 56–61.

Hughes, D. W. 1978. A Disaggregation and Thin Section Analysis of the Size and Mass Distribution of the Chondrules in the Bjurbole and Chainpur Meteorites. *Earth and Planetary Science Letters* 38: 391–400.

Jacquet, E. 2021. Collisions and Compositional Variability in Chondrule-Forming Events. *Geochimica et Cosmochimica Acta* 296: 18–37.

Jacquet, E., Paulhiac-Pison, M., Alard, O., Kearsley, A. T., and Gounelle, M. 2013. Trace Element Geochemistry of CR Chondrite Metal. *Meteoritics & Planetary Science* 48: 1981–99.

Jones, R. H. 2012. Petrographic Constraints on the Diversity of Chondrule Reservoirs in the Protoplanetary Disk. *Meteoritics & Planetary Science* 47: 1176–90.

Kapur, J. N., Sahoo, P. K., and Wong, A. K. 1985. A New Method for Gray-Level Picture Thresholding Using the Entropy of the Histogram. *Computer Vision, Graphics, & Image Processing* 29: 273–85.

Ketcham, R. A. 2005. Computational Methods for Quantitative Analysis of Three-Dimensional Features in Geological Specimens. *Geosphere* 1: 32–41.

Ketcham, R. A. 2006. Accurate Three-Dimensional Measurements of Features in Geological Materials from X-Ray Computed Tomography Data. In *Advances in X-Ray Tomography for Geomaterials*, edited by J. Desrues, G. Viggiani, and P. Bésuelle, 143–8. London: ISTE Ltd.

Krot, A. 2019. Refractory Inclusions in Carbonaceous Chondrites: Records of Early Solar System Processes. *Meteoritics & Planetary Science* 54: 1647–91.

Krot, A. N., Scott, E. R., and Zolensky, M. E. 1995. Mineralogical and Chemical Modification of Components in CV3 Chondrites: Nebular or Asteroidal Processing? *Meteoritics* 30: 748–75.

Leitner, J., Vollmer, C., Floss, C., Zipfel, J., and Hoppe, P. 2016. Ancient Stardust in Fine-Grained Chondrule Dust Rims from Carbonaceous Chondrites. *Earth and Planetary Science Letters* 434: 117–28.

Leshin, L. A., Rubin, A. E., and McKeegan, K. D. 1997. The Oxygen Isotopic Composition of Olivine and Pyroxene from CI Chondrites. *Geochimica et Cosmochimica Acta* 61: 835–45.

Leya, I., Schönbächler, M., Krahenbühl, U., and Halliday, A. N. 2009. New Titanium Isotope Data for Allende and Efremovka CAIs. *The Astrophysical Journal* 702: 1118–26.

Libourel, G., Krot, A. N., and Tissandier, L. 2006. Role of Gas-Melt Interaction during Chondrule Formation. *Earth and Planetary Science Letters* 251: 232–40.

Marrocchi, Y., Villeneuve, J., Batanova, V., Piani, L., and Jacquet, E. 2018. Oxygen Isotopic Diversity of Chondrule Precursors and the Nebular Origin of Chondrules. *Earth and Planetary Science Letters* 496: 132–41.

MBDB. 2022. Meteoritical Bulletin Database.

Metzler, K. 2018. From 2D to 3D Chondrule Size Data: Some Empirical Ground Truths. *Meteoritics & Planetary Science* 53: 1489–99.

Metzler, K., Bischoff, A., and Stöffler, D. 1992. Accretionary Dust Mantles in CM Chondrites: Evidence for Solar Nebula Processes. *Geochimica et Cosmochimica Acta* 56: 2873–97.

Metzler, K., Hezel, D. C., and Nellesen, J. 2019. Various Size-Sorting Processes for Millimeter-Sized Particles in the Sun's Protoplanetary Disk? Evidence from Chondrules in Ordinary Chondrites. *The Astrophysical Journal* 887: 230.

Millner, M. R., Payne, W. H., Waggener, R. G., McDavid, W. D., Dennis, M. J., and Sank, V. J. 1978. Determination of Effective Energies in CT Calibration. *Medical Physics* 5: 543–5.

Nagahara, H. 1981. Evidence for Secondary Origin of Chondrules. *Nature* 292: 135–6.

Patzer, A., Bullock, E. S., and Alexander, C. M. 2021. Testing Models for the Compositions of Chondrites and their Components: I. CO Chondrites. *Geochimica et Cosmochimica Acta* 304: 119–40.

Piralla, M., Villeneuve, J., Schnuriger, N., Bekaert, D. V., and Marrocchi, Y. 2023. A Unified Chronology of Dust Formation in the Early Solar System. *Icarus* 394: 115427.

Regnault, M., Marrocchi, Y., Piralla, M., Villeneuve, J., Batanova, V., Schnuriger, N., and Jacquet, E. 2022. Oxygen Isotope Systematics of Chondrules in Rumuruti Chondrites: Formation Conditions and Genetic Link with Ordinary Chondrites. *Meteoritics & Planetary Science* 57: 122–35.

Roth, A. S., Metzler, K., Baumgartner, L. P., and Leya, I. 2016. Cosmic-Ray Exposure Ages of Chondrules. *Meteoritics & Planetary Science* 51: 1256–67.

Rubin, A. E. 2010. Physical Properties of Chondrules in Different Chondrite Groups: Implications for Multiple Melting Events in Dusty Environments. *Geochimica et Cosmochimica Acta* 74: 4807–28.

Russell, S. S., Krot, A. N., Huss, G. R., Keil, K., Itoh, S., Yurimoto, H., and MacPherson, G. J. 2005. The Genetic Relationship Between Refractory Inclusions and Chondrules. In *Chondrites and the Protoplanetary Disk*,

edited by A. N. Krot, E. R. D. Scott, and B. Reipurth, vol. 341, 317. San Francisco: Astronomical Society of the Pacific.

Schindelin, J., Arganda-Carreras, I., Frise, E., Kaynig, V., Longair, M., Pietzsch, T., Preibisch, S., et al. 2012. Fiji: An Open-Source Platform for Biological-Image Analysis. *Nature Methods* 9: 676–82.

Schneider, J. M., Burkhardt, C., Marrocchi, Y., Brennecka, G. A., and Kleine, T. 2020. Early Evolution of the Solar Accretion Disk Inferred from Cr-Ti-O Isotopes in Individual Chondrules. *Earth and Planetary Science Letters* 551: 116585.

Schönbächler, M., and Fehr, M. 2013. Basics of Ion Exchange Chromatography for Selected Geological Applications. In *Treatise on Geochemistry. Vol. 15: Analytical Geochemistry/Inorganic Instrument Analysis*, edited by W. F. McDonough, 124–46. Amsterdam: Elsevier.

Schrader, D. L., Connolly, H. C., and Lauretta, D. S. 2008. Opaque Phases in Type-II Chondrules from CR2 Chondrites: Implications for CR Parent Body Formation. *Geochimica et Cosmochimica Acta* 72: 6124–40.

Scott, E. R., and Jones, R. H. 1990. Disentangling Nebular and Asteroidal Features of CO3 Carbonaceous Chondrite Meteorites. *Geochimica et Cosmochimica Acta* 54: 2485–502.

Trinquier, A., Elliott, T., Ulfbeck, D., Coath, C., Krot, A. N., and Bizzarro, M. 2009. Origin of Nucleosynthetic Isotope Heterogeneity in the Solar Protoplanetary Disk. *Science* 324: 374–6.

Tsuchiyama, A., Nakano, T., Uesugi, K., Uesugi, M., Takeuchi, A., Suzuki, Y., Noguchi, R., et al. 2013. Analytical Dual-Energy Microtomography: A New Method for Obtaining Three-Dimensional Mineral Phase Images and its Application to Hayabusa Samples. *Geochimica et Cosmochimica Acta* 116: 5–16.

Uesugi, M., Uesugi, K., and Oka, M. 2010. Non-destructive Observation of Meteorite Chips Using Quantitative Analysis of Optimized X-Ray Micro-Computed Tomography. *Earth and Planetary Science Letters* 299: 359–67.

Uesugi, M., Uesugi, K., Takeuchi, A., Suzuki, Y., Hoshino, M., and Tsuchiyama, A. 2013. Three-Dimensional Observation of Carbonaceous Chondrites by Synchrotron Radiation X-Ray CT—Quantitative Analysis and Developments for the Future Sample Return Missions. *Geochimica et Cosmochimica Acta* 116: 17–32.

Van Geet, M., Swennen, R., and Wevers, M. 2000. Quantitative Analysis of Reservoir Rocks by Microfocus X-Ray Computerised Tomography. *Sedimentary Geology* 132: 25–36.

van Kooten, E., and Moynier, F. 2019. Zinc Isotope Analyses of Singularly Small Samples (<5 Ng Zn): Investigating Chondrule-Matrix Complementarity in Leoville. *Geochimica et Cosmochimica Acta* 261: 248–68.

van Kooten, E., Schiller, M., Moynier, F., Johansen, A., Haugbølle, T., and Bizzarro, M. 2021. Hybrid Accretion of Carbonaceous Chondrites by Radial Transport across the Jupiter Barrier. *The Astrophysical Journal* 910: 70.

van Kooten, E. M., Schiller, M., and Bizzarro, M. 2017. Magnesium and Chromium Isotope Evidence for Initial Melting by Radioactive Decay of ^{26}Al and Late Stage Impact-Melting of the Ureilite Parent Body. *Geochimica et Cosmochimica Acta* 208: 1–23.

van Kooten, E. M., Wielandt, D., Schiller, M., Nagashima, K., Thomen, A., Larsen, K. K., Olsen, M. B., Nordlund, A., Krot, A. N., and Bizzarro, M. 2016. Isotopic Evidence for Primordial Molecular Cloud Material in Metal-Rich Carbonaceous Chondrites. *Proceedings of the National Academy of Sciences of the United States of America* 113: 2011–6.

Varley, L. R., Leshin, L. A., Guan, Y., Zanda, B., and Bourot-Denise, M. 2003. Oxygen Isotopic Composition of Renazzo Chondrule Olivine and Comparison with Extent of Chondrule Melting In Lunar and Planetary Science, p. 1899.

Villeneuve, J., Marrocchi, Y., and Jacquet, E. 2020. Silicon Isotopic Compositions of Chondrule Silicates in Carbonaceous Chondrites and the Formation of Primordial Solids in the Accretion Disk. *Earth and Planetary Science Letters* 542: 116318.

Wasson, J. T., Krot, A. N., Lee, M. S., and Rubin, A. E. 1995. Compound Chondrules. *Geochimica et Cosmochimica Acta* 59: 1847–69.

Wasson, J. T., and Rubin, A. E. 2010. Metal in CR Chondrites. *Geochimica et Cosmochimica Acta* 74: 2212–30.

Williams, C. D., Sanborn, M. E., Defouilloy, C., Yin, Q. Z., Kita, N. T., Ebel, D. S., Yamakawa, A., and Yamashita, K. 2020. Chondrules Reveal Large-Scale Outward Transport of Inner Solar System Materials in the Protoplanetary Disk. *Proceedings of the National Academy of Sciences of the United States of America* 117: 23426–35.

Williams, N. H., Fehr, M. A., Parkinson, I. J., Mandl, M. B., and Schönbächler, M. 2021. Titanium Isotope Fractionation in Solar System Materials. *Chemical Geology* 568: 120009.

Zanda, B., Humayun, M., and Hewins, R. H. 2012. Chemical Composition of Matrix and Chondrules in Carbonaceous Chondrites: Implications for Disk Transport 43rd Lunar and Planetary Science Conference, abstract #2413, The Woodlands, TX, p. 1659.

Zanda, B., Humayun, M., Lewin, E., Pont, S., and Hewins, R. H. 2018. Mo-W Isotopic Evidence Against Chondrule-Matrix Complementarity. In 81st Annual Meeting of the Meteoritical Society, LPI Contribution No. 2067, Moscow, Russia, p. 6171.

Zanda, C. B., Bourot-Denise, M., Hewins, R. H., Cohen, B. A., Delaney, J. S., Humayun, M., and Campbell, A. J. 2002. Accretion Textures, Iron Evaporation and Re-Condensation in Renazzo. 33rd Lunar and Planetary Science Conference, abstract #1852.

Zou, W., Nakashima, T., Onishi, Y., Koike, A., Shinomiya, B., Morii, H., Neo, Y., Mimura, H., and Aoki, T. 2008. Atomic Number and Electron Density Measurement Using a Conventional X-Ray Tube and a CdTe Detector. *Japanese Journal of Applied Physics* 47(9 Part 1): 7317–23.

APPENDIX A
CHONDRULE MIDPLANE ANALYSIS

Similar to the ground truth work performed on whole chondrites (i.e., Ebel et al., 2008; Elangovan et al., 2012) or single chondrules (i.e., Beitz et al., 2013), the accuracy of micro-XCT for chondrule metal analysis

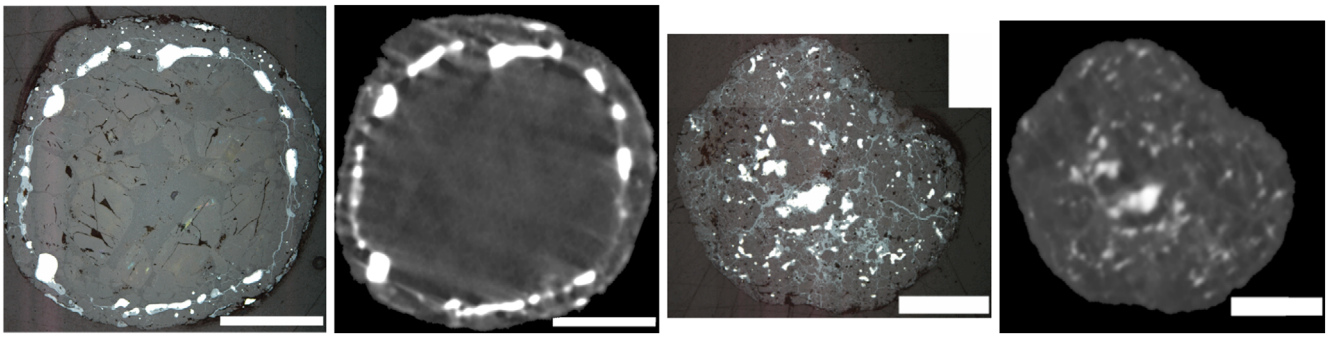

FIGURE A1. Reflected light image with the corresponding XCT slice. Depicted on the left is a porphyritic chondrule with a clearly differentiated metal rim and opaques surrounding said metal. On the right is a "rim-less" chondrule with evenly distributed metal and opaques. The scale bar on each image represents 500 μm. In the XCT images, the background (black) was removed for better visibility. (Color figure can be viewed at wileyonlinelibrary.com)

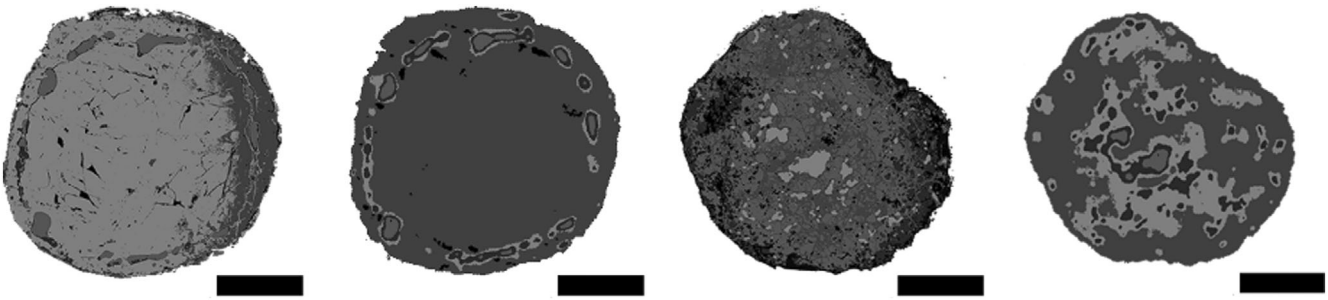

FIGURE A2. Phase map results of PhaseQuant on reflected light image compared to XCT. Gray values are arbitrary. Reflected light image shows minor artifacts due to the process of joining several images. The scale bar represents 500 μm.

is evaluated based on the XCT data and reflected light images of chondrule midplanes from Bjurböle (Bj1 and Bj2). The chondrule Bj1 has its metal concentrated in a rim, while Bj2 displays a more even metal distribution (Figure A1). The chondrules of interest were inserted into a solid epoxy cylinder together with their sample holder to maintain the same orientation as in the previously obtained, corresponding XCT image stack. The position in the stack was identified to an uncertainty of one layer (±5.3 μm). The chondrules in epoxy were manually ground down to their midplanes and polished using diamond paste. Opaque contents in the reflected light images and the corresponding XCT image were determined in area% using FIJI as in X-Ray Computed Tomography Section. The threshold for the reflected light images was set manually to include all metal (white under reflected light).

For phase separation, we used PhaseQuant with the Kmeans clustering method. In the case of Bj1, the auto-threshold method MaxEntropy of FIJI was applied, resulting in a good separation of low-attenuating silicates from the high-attenuating opaques (Elangovan et al., 2012). In the case of Bj2, the threshold was set manually, coinciding with the auto-threshold used for Bj1. In addition to the incapability of using an auto-threshold for Bj2-type chondrules, we found that XCT cannot differentiate well between metal and non-metal opaques (oxides and sulfides) if the latter are cross-cutting silicates and metal (Figure A2, Table A1). Chondrules with large metal nodules yield metal contents in a single XCT slice broadly in agreement with the metal content measured under reflected light (underestimate by 14%; Table A1). Large contents of small metal nodules as found in Bj2 and chondrules labeled "rim-less" lead to

TABLE A1. Calculated metal content using PhaseQuant from X-ray computed tomography (XCT) slice of two Bjurböle chondrules (Bj1 and Bj2) compared to the reflected light (RL) image taken at the same depth within the chondrule.

Name	Metal (area%)	Other opaques (area %)	Total (area %)
Bj1 (RL)	4.5	2.8	7.22
Bj1 (XCT)[a]	3.9 ± 0.3	1.9 ± 0.1	6.8 ± 0.3
Bj2 (RL)	13.4	27.1	40.5
Bj2 (XCT)[a]	1.1 ± 0.1	8.3 ± 0.3	9.4 ± 0.2

[a]Standard deviation of metal content over three adjacent XCT slices.

a strong underestimate (90%) of the chondrule's opaque content. If nodules become smaller and reach sizes close to the voxel resolution, as observed in Bj2, partial volume effects (Hanna & Ketcham, 2017; Ketcham, 2006) lead to more voxels being mistaken as silicates instead of opaques. In contrast, shadowing and starburst artifacts (De Man et al., 1999; Hanna & Ketcham, 2017) cause silicates to be mistaken for non-metal opaques. For XCT metal content estimates overall, the results can therefore be representative (Bj1) or deviate by an order of magnitude (Bj2) when compared to reflected light image metal contents. Any metal content reported in this work is thus an underestimation, whereas metal contents for chondrules with large amounts of randomly distributed, small metal nodules are not representative and therefore not reported.

APPENDIX B
CHONDRULE DATA TABLES

The results of the micro-XCT analysis are summarized in Tables B1–B8. This includes the chondrule type and texture (type), metal content (metal), diameter (/), density (ρ) and features. For features, abbreviations were used: metal rim (m), double metal rim (m + m), igneous rim (i) matrix on rim (ma), and compound chondrule (cc). The chondrule texture short forms are: P—porphyritic, MP—microporphyritic, B—barred, R—radial. The "rim-less" short form is used for the texture of weakly processed chondrules with evenly distributed metal nodules obscuring the texture. Non-chondrule samples composed of matrix material or pure metal are labeled as "matrix" and "metal," respectively.

TABLE B1. Jbilet Winselwan (CM2) chondrule tomography results.

#	Type, texture[a]	Metal (vol%)	Ø (mm)	ρ (g cm^{-3})	Features[b]	
01	I, B[c]	0.0	0.6	3.1		
02	I, ?	0.0	0.4	3.0		
03	I, ?	0.0	0.4	3.0		
04	I, ?	0.0	0.4	3.0		
05	I, ?	0.0	0.3	3.0		
06	I, ?	0.0	0.3	3.0	m[c]	
07	I, ?	0.0	0.6	3.1	m	ma
08	I, P	0.0	0.5	3.1		
09	I, ?	0.0	0.3	3.0		

[a]Type I expresses LAC of Ol (Fa < 10%), type II (Fa > 10%); texture: P—porphyritic; B—barred.
[b]Metal rim (m), matrix on rim (ma).
[c]Tentative.

TABLE B2. Allende (CV3) tomography results.

#	Type, texture[a]	Metal (vol%)	Ø (mm)	ρ (g cm^{-3})	Features[b]		
01	I, rim-less[c]	<0.1	0.7	3.3			
02	I, P	0.1	0.6	3.4			
03	I, P	0.0	0.5	3.2	m		
04	I, P	0.0	0.5	3.3	m	cc[c]	
05	I, P	0.3	0.6	3.3	m		
06	I, ?	0.0	0.5	3.2		cc[c]	
07	I, P	<0.1	0.5	3.3			
08	I, P[d]	<0.1	1.0	3.1	m		ma[c]
09	I, P[c]	2.1	1.1	3.3	m		ma

[a]Type I expresses LAC of Ol (Fa < 10%), type II (Fa > 10%); texture: P—porphyritic, MP—microporphyritic, B—barred, R—radial; rim-less—evenly distributed metal obscuring texture.
[b]Metal rim (m), igneous rim (i), compound chondrule (cc), matrix on rim (ma).
[c]Tentative.
[d]Tabular mineral growth in center surrounded by granular minerals.

TABLE B3. Gujba (CBa) chondrule tomography results.

#	Type, texture[a]	Metal (vol%)	Ø (mm)	ρ (g cm^{-3})	Features[b]
01	I, ?	4.0	16.6[c]	3.3	
02	I, ?	1.1	11.9[d]	3.1	ma
03	I, ?	<0.1	9.3[e]	3.1	
04	I, ?	<0.1	10.3	3.1	
05	I, ?	0.0	9.8	3.1	
06	I, ?	<0.1	9.3	3.1	
07	I, ?	3.5	16.2	3.3	
08	I, ?	0.0	8.2	3.0	
09	I, ?	<0.1	11.0	3.1	

[a]Type I expresses LAC of Ol (Fa < 10%), type II (Fa > 10%).
[b]Matrix on rim (ma).
[c]Three fragments, chondrule diameter only for volume.
[d]Four fragments, chondrule diameter only for volume.
[e]Six fragments, chondrule diameter only for volume.

TABLE B4. PCA 91020 (EL3) chondrule tomography results.

#	Metal (vol%)	Ø (mm)	ρ (g cm^{-3})
01	66.4	1.1	5.0
02	70.2	1.1	5.6
03	62.1	0.9	4.8
04	67.2	0.8	5.2
05	76.7	0.8	5.6
06	71.1	0.7	5.3
07	61.6	0.4	4.4
08	77.0	0.6	5.5
09	82.1	0.7	5.8
10	77	0.6	5.5
11	74.9	0.4	5.7

Type, texture column was omitted because neither type nor texture could be determined.

TABLE B5. QUE 97008 (L3.05) chondrule tomography results.

#	Type, texture[a]	Metal (vol%)	Ø (mm)	ρ (g cm^{-3})	Features[b]			
01	I, MP[c]	0.0	1.5	3.3				
02	II, R[c]	0.0	1.0	3.3				
03	I, ?	0.0	0.6	3.2				
04	II, R[c]	0.0	1.3	3.3		i		
05	II, ?	<0.1	1.4	3.3				
06	II, R	<0.1	1.5	3.3				
07	I, ?	0.0	1.0	3.1				
08	II, ?	<0.1	1.0	3.3				ma
09	II, ?	<0.1	1.0	3.4	m			ma
10	I, B[c]	<0.1	0.8	3.2				
11	Matrix[d]	1.6	0.8	3.5	—	—	—	—
12	I, MP[c]	<0.1	0.7	3.2				
13	I, ?	0.0	0.6	3.1				
14	Matrix[d]	—	1.0	3.3	—	—	—	—
15	II, P	<0.1	1.2	3.2	m			
16	I, ?	1.0	1.0	3.3	m			ma[d]
17	I, ?	1.4	1.2	3.1	m + m			ma[d]
18	I, ?	1.1	1.0	3.3		i[c]		

[a]MP—microporphyritic, B—barred, R—radial; matrix—sample made up of matrix material.
[b]Metal rim (m), double metal rim (m + m), igneous rim (i), matrix on rim (ma).
[c]Tentative.
[d]Chondrules fragments within matrix.

TABLE B6. EET 92048 (CR2) chondrule tomography results.

#	Type, texture[a]	Metal (vol%)	Ø (mm)	ρ (g cm^{-3})	Features[b]			
01	I, P	1.8	1.8	3.5	m	i	cc	
02	I, ?	1.4	0.9	3.3				
03	I, ?	7.8	1.8	3.5	m	i		
04	I, ?	<0.1	0.8	3.1				
05	I, ?	4.1	1.8	3.5	m		cc	
06	I, ?	6.3	1.2	3.4	m			
07	I, P[c]	12.0	2.3	3.7	m + m			
08	I, P[c]	2.4	2.5	3.5		i		
09	I, P[c]	2.6	1.0	3.5	m		cc[d]	
10	I, P	0.0	0.9	3.1				
11	I, P	0.0	1.1	3.1				
12	I, P	2.6	1.7	3.4	m		cc	ma
13	I, ?	3.8	1.4	3.3				
14	I, P	2.4	1.4	3.3	m			ma
15	I, ?	2.6	1.4	3.3	m		cc[d]	ma
16	Opaques	—	1.4	5.2	—	—	—	—
17	I, rim-less	—	1.3	3.4				ma[c]
18	I, P[c]	5.2	1.1	3.4	m			ma[c]
19	I, ?	15.1	1.3	4.0				
20	I, P[c]	4.4	1.1	3.3	m		cc[d]	ma
21	I, rim-less	—	1.0	3.4				
22	I, P	0.4	0.9	3.1				
23	Opaques	—	1.0	5.1	—	—	—	—
24	I, ?	3.0	0.9	3.2	m			ma[c]
25	I, ?	8.9	0.1	3.4	m + m			
26	Opaques	—	0.9	4.8	—	—	—	—
27	I, ?	12.7	0.8	3.3	m			
28	I, ?	2.3	0.8	3.2				
29	Opaques	—	0.7	4.8	—	—	—	—
30	I, P	8.2	1.6	3.4	m			
31	I, P	9.6	1.8	3.5	m	i		
32	I, ?	2.4	1.2	3.3				
33	I, ?	1.4	1.8	3.4		i		
34	I, rim-less[c]	—	1.2	3.3				
35	I, P[c]	27.9	1.2	3.7	m			
36	II, P	<0.1	1.0	3.3				
37	Matrix	—	1.3	3.4	—	—	—	—
38	I, ?	2.3	1.3	3.4	m	i	cc[d]	
39	I, ?	4.7	1.3	3.4	m	i		
40	I, ?	3.6	1.1	3.3				
41	I, ?	1.4	1.1	3.3	m			
42	Opaques	—	1.0	4.3	—	—	—	—
43	Opaques	—	1.1	4.4	—	—	—	—
44	I, ?	1.9	0.9	3.3				
45	Opaques	—	0.9	4.6	—	—	—	—
46	Opaques	—	0.2	4.3	—	—	—	—

[a]Type I expresses LAC of Ol (Fa < 10%), type II (Fa > 10%); texture: MP—microporphyritic, B—barred, R—radial; matrix—sample made up of matrix material, rim-less—evenly distributed opaques obscuring texture, opaques—sample does not contain distinguishable silicates.
[b]Opaques rim (m), double opaques rim (m + m), igneous rim (i), compound chondrule (cc), matrix on rim (ma).
[c]Tentative.
[d]Chondrules separated by matrix.

TABLE B7. GRA 06100.33 (CR2) chondrule tomography results.

#	Type, texture[a]	Metal (vol%)	Ø (mm)	ρ (g cm^{-3})	Features[b]			
01	I, P	2.4	1.4	3.3	m			
02	Matrix	—	1.3	3.5	—	—	—	—
03	Matrix	—	1.4	3.8	—	—	—	—
04	I, P	0.9	1.6	3.4	m	i		ma[d]
05	I, ?	0.0	1.7	3.5	m	i		ma
06	I, P	1.5	1.9	3.3	m			ma[c]
07	I, P[c]	3.9	1.1	3.4	m			
08	I, ?	2.4	1.1	3.4	m + m			
09	I, P	<0.1	0.9	3.2	m			
10	I, ?	0.6	0.6	3.3	m			
11	I, ?	0.3	0.7	3.2	m			ma
12	I, P[c]	2.0	1.3	3.4	m	i		ma
13	I, P	2.9	1.0	3.2	m			
14	I, ?	<0.1	0.8	3.4			cc[e]	
15	I, P	2.9	1.5	3.4	m			
16	Matrix	—	1.1	3.7	—	—	—	—
17	I, ?	2.5	1.1	3.4	m			
18	I, P	<0.1	0.9	3.1	m			
19	I, ?	<0.1	0.8	3.3				
20	I, ?	0.7	0.6	3.3	m			
21	I, ?	<0.1	0.5	3.2	m			
22	Metal	—	0.6	5.3	—	—	—	—
23	I, P	<0.1	0.8	3.2	m			ma[c]
24	I, P[c]	0.8	0.8	3.2	m			
25	I, P	0.9	0.7	3.3	m		cc[e]	ma
26	I, P[c]	1.4	0.7	3.3	m		cc[e]	
27	I, P	<0.1	0.6	3.2	m			
28	I, ?	2.0	0.6	3.4				ma
29	Metal	—	0.6	4.6	—	—	—	—

[a]Type I expresses LAC of Ol (Fa < 10%), type II (Fa > 10%); texture: MP—microporphyritic, B—barred, R—radial; matrix—sample made up of matrix material, pristine—evenly distributed metal obscuring texture, metal—sample does not contain distinguishable silicates.
[b]Metal rim (m), double metal rim (m + m), igneous rim (i), matrix on rim (ma).
[c]Tentative.
[d]Whole chondrule and chondrule fragment separated by matrix.
[e]Chondrules separated by matrix.

TABLE B8. Shişr 033 (CR) chondrule tomography results.

#	Type, texture[a]	Metal (vol%)	Ø (mm)	ρ (g cm^{-3})	Features[b]			
01	I, P	0.3	2.5	3.3	m			
02	I, ?	<0.1	2.0	3.3				ma[c]
03	I, P[c]	<0.1	1.5	3.2				ma
04	I, P[c]	<0.1	1.9	3.2	m+m[c]			
05	I, P[c]	0.3	2.2	3.4	m			ma
06	I, P	<0.1	1.3	3.2	m			
07	I, R[c]	<0.1	1.5	3.2	m			
08	I, ?	<0.1	1.4	3.3		i[c]		ma[c]
09	I, P	<0.1	1.6	3.2	m			
10	II, P	0.2	1.5	3.4	m			
11	I, P	0.5	1.4	3.3	m			ma
12	I, MP[c]	0.0	1.3	3.2				
13	I, P[c]	0.5	3.0	3.4	m	i[e]	cc[d]	
14	I, ?	1.5	2.8	3.3		i[c]		
15	I, MP[c]	<0.1	1.9	3.4		i[c]		
16	II[f], ?	6.7	1.5	3.8		i[c]		
17	I, P[c]	<0.1	1.4	3.2				
18	I, ?	0.3	1.3	3.2				
19	I, ?	0.6	1.3	3.2				
20	II, ?	<0.1	1.2	3.4				
21	I, ?	<0.1	1.0	3.2	m			

[a]Type I expresses LAC of Ol (Fa < 10%), type II (Fa > 10%); texture: MP—microporphyritic, B—barred, R—radial; matrix—sample made up of matrix material, pristine—evenly distributed metal obscuring texture, metal—sample does not contain distinguishable silicates.
[b]Metal rim (m), double metal rim (m + m), igneous rim (i), matrix on rim (ma).
[c]Tentative.
[d]Chondrules separated by matrix.
[e]Rim is 33% of chondrule volume.
[f]Might not be a chondrule. LAC lies between silicates and metals. Could be sulfide or oxidized metal as in Shişr#14.